Bio-Design and Manufacturing (2024) 7:983–999
https://doi.org/10.1007/s42242-024-00287-1

RESEARCH ARTICLE

$Ca_v3.3$-mediated endochondral ossification in a three-dimensional bioprinted GelMA hydrogel

Zhi Wang[1] · Xin Wang[1] · Yang Huang[2] · Junjun Yang[3] · Zu Wan[1] · Zhenlan Fu[1] · Xiaoyuan Gong[1] · Guangxing Chen[1] · Liu Yang[1]

Received: 21 November 2023 / Accepted: 8 May 2024 / Published online: 26 November 2024

Abstract

The growth plate (GP) is a crucial tissue involved in skeleton development via endochondral ossification (EO). The bone organoid is a potential research model capable of simulating the physiological function, spatial structure, and intercellular communication of native GPs. However, mimicking the EO process remains a key challenge for bone organoid research. To simulate this orderly mineralization process, we designed an in vitro sh$Ca_v3.3$ ATDC5-loaded gelatin methacryloyl (GelMA) hydrogel model and evaluated its bioprintability for future organoid construction. In this paper, we report the first demonstration that the T-type voltage-dependent calcium channel (T-VDCC) subtype $Ca_v3.3$ is dominantly expressed in chondrocytes and is negatively correlated with the hypertrophic differentiation of chondrocytes during the EO process. Furthermore, $Ca_v3.3$ knockdown chondrocytes loaded with the GelMA hydrogel successfully captured the EO process and provide a bioink capable of constructing layered and orderly mineralized GP organoids in the future. The results of this study could therefore provide a potential target for regulating the EO process and a novel strategy for simulating it in bone organoids.

✉ Xiaoyuan Gong
sliegxy@foxmail.com

✉ Guangxing Chen
cgx7676@hotmail.com

✉ Liu Yang
jointsurgery@163.com

[1] Chongqing Key Laboratory of Precision Medicine in Joint Surgery, Center for Joint Surgery, Southwest Hospital, Army Medical University (Third Military Medical University), Chongqing 400038, China

[2] Department of Pharmacy and Laboratory Medicine, Army Medical University (Third Military Medical University), Chongqing 400038, China

[3] Key Laboratory of Biorheological Science and Technology, Ministry of Education, College of Bioengineering, Chongqing University, Chongqing 400044, China

Graphic abstract

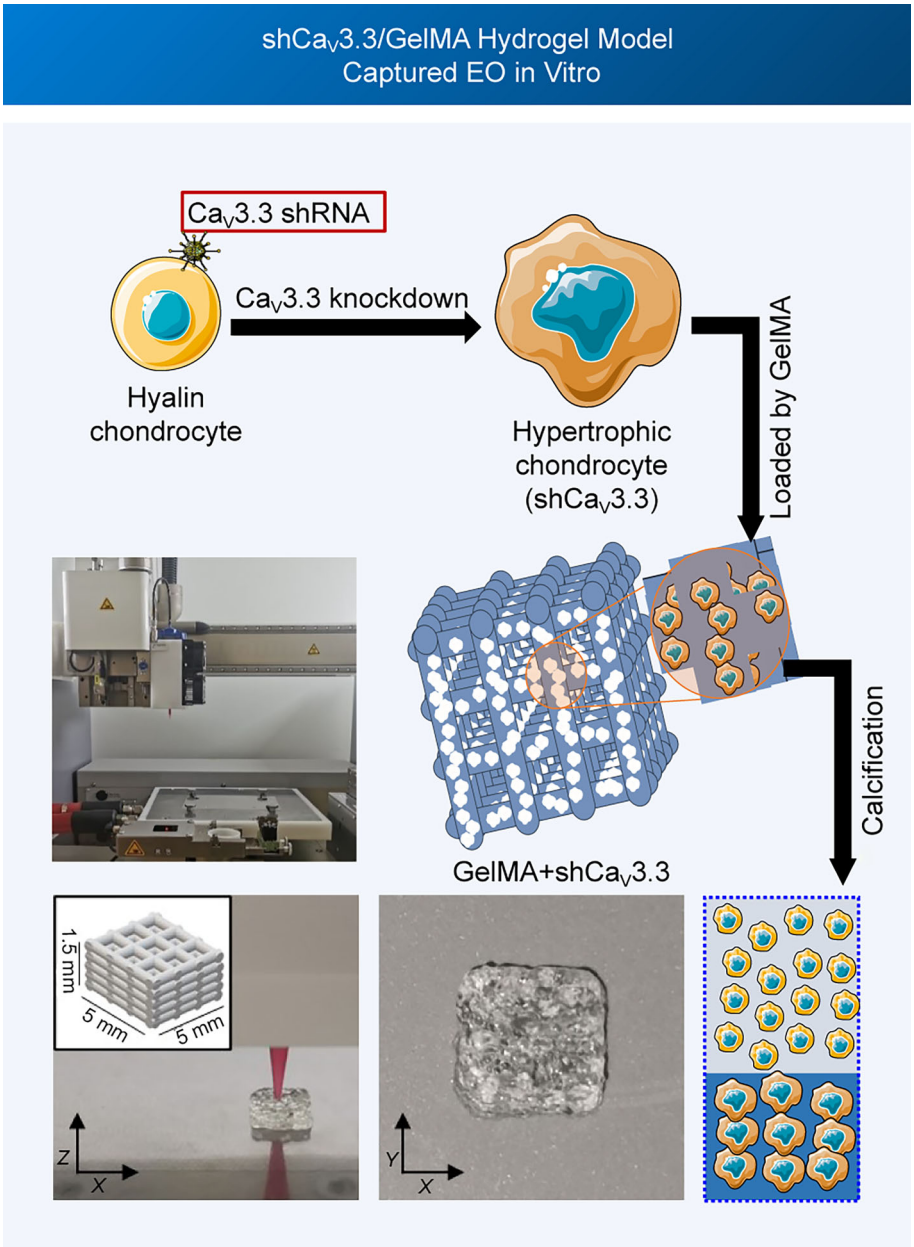

Keywords Bone organoid · Endochondral ossification · T-type voltage-dependent calcium channel (T-VDCC) · $Ca_v3.3$ · 3D bioprinting

Introduction

The growth plate (GP) is a unique tissue located at the metaphysis and is responsible for the postnatal elongation of long bones. However, GP dysfunctions can lead to growth retardation and campomelic dysplasia. However, studies of the physiological and pathological functions of the GP are restricted by its complicated spatiotemporal transformation, which is difficult to monitor in vivo or replicate in vitro [1–5]. Recently, the development of three-dimensional (3D) bioprinting techniques has enabled bone organoids to provide a valuable in vitro research model for studying the physiological and pathological functions of GP by simulating the structural and biological characteristics of native tissues [5, 6].

The main challenge regarding bone organoids involves mimicking the endochondral ossification (EO) process [7–9], which is the key process of GP maturation [10]. EO is tightly regulated by various factors, including transcription factors, soluble mediators, extracellular matrices, as well as cell—cell and cell–matrix interactions. Moreover, during EO the phenotype of chondrocytes transforms from hyaline chondrocytes in the resting zone to hypertrophic chondrocytes in the hypertrophic zone [11, 12]. Hence, orchestrated regulation of various genes and proteins and the subsequent elongation of long bone by ordered mineralization are key for successful EO simulation in bone organoids. To target spatial–temporal cellular function during the EO process, controlling the differentiation of chondrocytes into desirable differentiated stages is critical. Various strategies and/or methods have been proposed to induce lineage commitment of chondrocytes in bone organoids. However, despite recent advancements in tissue engineering, the replication of complex involvement in growth factors (e.g., Activin A, CHIR, fibroblast growth factor 2 (FGF2), PIK90, A8301, LDN, PD, purmorphamine, and transforming growth factor-beta 3 (TGF-β3)) and mechanical stimulation remains challenging [13, 14].

The electrophysiological microenvironment is an important physicochemical factor determining the development of osteochondral tissue. It affects chondrocyte differentiation by regulating the biological processes by which intracellular calcium signaling is initiated by voltage-dependent calcium channels (VDCCs) [15, 16]. Different VDCC subtypes recognize various membrane potentials and initiate intracellular calcium signaling via extracellular calcium influx and endoplasmic reticulum calcium release in chondrocytes [17–22]. A previous study by our group indicated that T-type VDCC (T-VDCC) blockages significantly reduced intracellular calcium signaling intensity and downregulated the expression levels of hyaline cartilage-related genes, thereby suggesting that T-VDCCs play an indispensable role during the activation of calcium signaling in chondrocytes [23]. In addition, other studies have demonstrated that the maintenance of chondrocyte phenotypes is regulated by VDCCs [18, 22]. Hence, we hypothesized that T-VDCCs may play an important role in the hypertrophic differentiation of chondrocytes.

In this study, we evaluated the key regulatory role of the T-VDCC subtype $Ca_v3.3$ in hypertrophic differentiation during EO, aiming to mimic the regulatory mechanism observed in GP maturation. In addition, we preliminarily validated the hypothesis that $Ca_v3.3$ regulates ordered mineralization in bone organoids by constructing bio-printable gelatin methacryloyl (GelMA) hydrogel loaded with $Ca_v3.3$ specifically knockdown ATDC5 cells.

Materials and methods

Animals

Twelve C57BL/6 mice (provided by the experimental animal center of Third Military Medical University; specific pathogen-free, 1-month-old, $n = 3$; 2-month-old, $n = 3$; 4-month-old, $n = 3$; 6-month-old, $n = 3$) and nine *Cacna1i* [flox/flox, *Col2*-CreERT]*(Cacna1i*$^{-/-}$) C57BL/6 mice (purchased from Cyagen, China; specific pathogen-free, 2-month-old, $n = 3$; 4-month-old, $n = 3$; 6-month-old, $n = 3$) were used in this study. One-month-old C57BL/6 mice were used for chondrocyte isolation, as well as for investigation of the relative expression levels of T-VDCC subtypes in primary chondrocytes. GP-specific knockout of the $Ca_v3.3$ T-VDCC subtype was achieved via tamoxifen injection administered one month after birth. Animals were then divided into wild-type and *Cacna1i*$^{-/-}$ groups. Two groups were subjected to hematoxylin–eosin (H&E) and Safranin O/Fast Green staining to observe the development of the GP.

Primary chondrocyte isolation and cell culture

After killing, the articular cartilage of the femoral condyle was excised and disinfected in 75% ethanol for 5 min. Cartilage was then minced into 1 mm^3 pieces and digested in Dulbecco's modified Eagle medium (DMEM, Hyclone, USA) containing 0.2% type II collagenase (BioFroxx, China) for 12 h at 37 °C. Undigested tissue fractures were then removed using a 100-μm filter. Primary chondrocytes were isolated via centrifugation at 1000 r/min for 5 min, and then resuspended in DMEM (Hyclone, USA) supplemented with 5% fetal bovine serum (FBS; Gibco, USA) and 1% penicillin/streptomycin (Gibco, USA). Both ATDC5 cells (Biospes, China) and mouse primary chondrocytes were cultured in DMEM supplemented with 5% FBS and 1% penicillin/streptomycin at 37 °C in 5% CO_2. Cell splitting was performed when the cell culture reached 90% confluence.

$Ca_v3.3$ interference in ATDC5

To achieve stable inhibition of $Ca_v3.3$ expression in ATDC5, we constructed $Ca_v3.3$ to specifically knockdown ATDC5 ($shCa_v3.3$); to do so we infected cells with shRNA using HBLV-m-Cacna1i-shRNA-ZsGreen-PURO (HANBIO, China). The vehicle group was constructed by infecting ATDC5 with shRNA using HBLV-ZsGreen-PURO NC (HANBIO, China). The shRNA sequences used are listed in Table S1 (Supplementary Information). Green fluorescent protein (ZsGreen) conjugated shRNA was used to ensure successful insertion of the intervening sequence. The down-regulation of $Ca_v3.3$ expression was validated by quantitative reverse transcription polymerase chain reaction (qRT-PCR), Western blotting, and immunofluorescence staining (IF).

Bioink preparation

A GelMA hydrogel (degree of amino substitution (DAS): 60%) (EFL Company, China) was used to construct the scaffold, with all procedures following the manufacturer's protocol. Briefly, 2.5 mg/mL lithium phenyl-2,4,6-trimethylbenzoylphosphinate (LAP) initiator standard solution was prepared and added to a GelMA solid to form a 5% GelMA solution. After dissolution, this mixture was immediately sterilized using a 0.22-μm sterile syringe filter. Cells were then collected and resuspended in a preheated 37 °C GelMA hydrogel solution for further printing and/or analysis. The GelMA hydrogel-cell mixture was then added to a well plate and irradiated with 405 nm ultraviolet (UV) light for 10 s to initiate crosslinking. The two-layered hydrogel was fabricated with GelMA loaded with $shCa_v3.3$ on the bottom and GelMA loaded with ATDC5 in the supernatant. The resulting hydrogel was then cut into 5 mm × 5 mm pieces and placed on the upper chamber of a transwell plate to facilitate better nutrient exchange inside the hydrogel.

Rheological measurements of the bioink

To explore the printing parameters of GelMA, we performed a rheological test of a 5% GelMA hydrogel precursor solution using a rheometer (Discovery HR-20, USA), and included measurements of temperature, frequency, and strain sweep. A 40-mm-diameter plate-and-plate geometry was used for all measurements. For the GelMA solution, the gap size was 100 μm for all cases. Temperature control was maintained using bottom plate attachments with cooling supplied by a circulating chiller. After production, all results were recorded and analyzed using TRIOS software (version 5.5.1). Next, we recorded the storage modulus (G') and loss modulus (G'') from 5 to 37 °C. We then selected seven potential processing temperatures (i.e., 15, 17, 19, 21, 23, 25, and 27 °C) and confirmed their shear-thin behavior by torsion mode.

Bioink characterization analyses

To verify the mobility and coagulability of the bioink over a range of temperatures, a diffusion test was performed after hydrogel extrusion. Specifically, a hydrogel heated at 37 °C was added to a 1-mL syringe with a diameter of 0.45 mm. After rewarming to the specified temperature, 600 μL of the same hydrogel was extruded at a uniform speed, and static and dynamic morphologies were observed. The diffusion ability at different temperatures was then evaluated by comparing the diameters of the extruded material.

The swelling properties of GelMA were assessed using a weighing technique commonly employed for ion osmotic pressure liquid environment, including phosphate-buffered saline (PBS). Briefly, samples were first washed with 2 mL of PBS at 37 °C, and then sampled at intervals of 0, 2, 6, 12, and 24 h. Any excess liquid was eliminated using wax paper. Subsequently, a balance with a precision level of 0.1 mg was used to measure the weight after swelling (W_s). We then freeze-dried samples under vacuum conditions for 24 h before recording the final mass of the dried sample (W_d). The swelling ratio was then calculated as $(W_s - W_d)/W_s \times 100\%$. Statistical analysis was performed using three technical replicates from each group.

The in vitro degradation rate of GelMA hydrogel was evaluated by accelerating the degradation process using collagenase type II (BioFroxx, China). After rinsing with 2 mL PBS at 37 °C for 24 h and weighing, samples were immersed in PBS containing collagenase type II at a concentration of 2 U/mL. Subsequently, samples were collected at different time intervals (i.e., after 0, 1, 2, 4, and 6 h) before being subjected to freeze-drying. The weight of each sample after drying was recorded (W_{d0} for the initial time point and W_{dn} for subsequent time points). The in vitro mass degradation percentage was calculated using the formula $(W_{d0} - W_{dn})/W_{d0} \times 100\%$. A balance with a precision of 0.1 mg was used for all weight determinations. Finally, statistical analysis included three technical replicates from each group.

Three-dimensional bioprinting

Next, we performed 3D bioprinting. To do so, cells were first mixed with 5% GelMA hydrogel to construct 5 mm × 5 mm × 1.5 mm hydrogel blocks using a 3D-Bioplotter (EnvisionTEC, Germany) bioprinting system. Bioprinting took place at 15 °C with 1 bar (1 bar = 100 kPa) extrusion pressure and 7 mm/s extrusion speed, and after printing blocks were irradiated with 405 nm UV light for 10 s to enable crosslinking. After bioprinting, hydrogel blocks were placed in transwell plates supplemented with 600 μL of culture medium and were assessed cell viability immediately. The hydrogels were then cultured for 7 d, with the culture medium changed every

two days. Finally, cell attachment in the hydrogel was evaluated using scanning electron microscopy (SEM), with all experiments being performed in triplicate.

Immunofluorescence staining

Next, we used immunofluorescence staining to quantify the expression of three subtypes of T-VDCC proteins in mouse primary chondrocytes and ATDC5 and identify changes in chondrogenic/osteogenic differentiation-related markers of shCa_v3.3 under 3D culture. To do so, cells or hydrogels were first fixed with 4% paraformaldehyde for 15 min, and then washed thoroughly with PBS. Antigen blocking was performed using incubation with an immunohistochemistry blocking solution at room temperature (RT) for 2 h. After removing the blocking solution, anti-Ca_v3.3, RUNX-2 (Santa, USA), COL-II, SOX-9, ACAN, COL-X, and MMP-13 (Affinity, China) antibodies were added and incubated overnight at 4 °C. Samples were then washed three times with PBS-Tween 20 (PBST) before Alexa Fluor 555-labeled donkey anti-mouse IgG(H + L) or Alexa Fluor 555-labeled donkey anti-rabbit IgG(H + L) (Beyotime, China) antibodies were added and incubated at RT for 1 h. Finally, samples were washed three times with PBST (5 min each time), followed by staining with 4',6-diamidino-2-phenylindole (DAPI) for 10 min. After washing with PBST, the samples were observed using an LSM780 laser confocal microscope (ZEISS, Germany).

Analysis of differentiated markers within the hydrogel

Next, to detect the expression of chondrocyte differentiation-related markers in 3D culture, cells were isolated from the hydrogel using a 0.3 mg/mL GelMA hydrogel digesting solution, which was mainly composed of collagenase crude extract (EFL Company, China). The cell precipitate was obtained by centrifugation at 1000 r/min for 5 min for subsequent Western blotting and mRNA sequencing analyses.

Next, total RNA was extracted from ATDC5 and shCa_v3.3 cells using TRIzol reagent (Invitrogen, USA). Total RNA was then quantified and reverse transcribed into cDNA using a reverse transcription kit (Toyobo, Japan). Briefly, the cDNA template, primers, and fluorescent probe were added to PCR reaction tubes along with PCR Master Mix (Toyobo, Japan). qRT-PCR reactions were performed in triplicate in 96-well plates using a real-time PCR system (Bio-Rad, CFX96, USA). The sequences of all primer pairs used are listed in Table S2 (Supplementary Information).

Finally, protein fractions were prepared using radioimmunoprecipitation assay (RIPA) Lysis Buffer (Beyotime, China), and 20 μg/lane of protein fraction solution was then subjected to sodium dodecyl sulfate–polyacrylamide gel electrophoresis (SDS-PAGE; 4%–15% polyacrylamide) (Beyotime, P0466S, China). After electrophoresis, gel membranes were incubated with anti-Ca_v3.3, RUNX-2 (Santa, USA), COL-II, SOX-9, ACAN, COL-X, MMP-13, and β-actin (Affinity, China) antibodies, followed by secondary incubation with goat anti-rabbit IgG (H + L) horseradish peroxidase (HRP) and goat anti-mouse IgG (H + L) HRP (1:5000 dilution; Affinity, China). An electrochemiluminescence detection kit (Amersham, UK), a ChemiDoc MP imaging system (BIO-RAD, USA), and a FUSION FX.EDGE SPECTRA System (VILBER BIO IMAGING, FR) were used to detect bound protein.

Calcium imaging

Next, $[Ca^{2+}]_i$ transients were monitored in ATDC5 using Fluo-4 acetoxymethyl ester (Fluo-4 AM) (Beyotime, China) and fluorescence microscopy (IX71; Olympus, Hamburg, Germany). Cells were first washed three times with PBS, and then loaded with calcium indicator (Fluo-4 AM, 5 μmol/L) at 37 °C for 30 min, after which excess dye was removed by washing three times with PBS. Fluorescent images of cells were recorded using a 4× objective at RT. To avoid error analyses in basal cytosolic Ca^{2+} levels when using a single wavelength calcium indicator, all $[Ca^{2+}]_i$ measurements were performed by fluorescence microscopy. All images were obtained using the same settings and were analyzed using the same parameters in ImageJ version 1.53k.

mRNA sequencing

Before conducting mRNA sequencing, total RNA was first extracted from ATDC5 and shCa_v3.3 cells cultured in either two-dimensional (2D) or 3D environments using aforementioned methods. For mRNA sequencing, RNA quality and quantity were assessed using agarose gel electrophoresis and a NanoPhotometer spectrophotometer. After RNA extraction, RNA was then ligated to an adaptor for further amplification using the NEBNext® Ultra™ RNA Library Prep kit (Illumina, USA). All library preparation was performed at Knorigene Technologies Co. Ltd. (China). The resulting libraries were then sequenced using a NovaSeq PE150 platform (Illumina, USA). After sequencing, quality control of raw sequencing data was performed using FastQC. Gene expression was calculated using featureCounts, and differentially expressed genes (DEGs) were identified using the R package DESeq2 [24]. To analyze differences in gene expression between ATDC5 and shCa_v3.3 cells or between 2D and 3D culture environments, mRNA sequencing was performed on different cell samples isolated from 2D and 3D cultures. DEGs ($P < 0.05$ & $\log_2$ fold Change >1 or <−1) were subjected to further analysis, including gene ontology (GO) enrichment analysis.

In situ proliferation analysis of the GelMA hydrogel

To verify that the viability of cells cultured in GelMA hydrogel after 1, 7, and 14 d of culturing, we stained cells using an 5-ethynyl-2-deoxyuridine (EdU) kit (Beyotime, China) with all procedures following the manufacturer's protocol. To do so, the GelMA hydrogel was immersed in the 2× EdU solution under sterile conditions at 37 °C for 2 h. Samples were fixed and permeabilized before being incubated with a click reaction solution for 30 min. Afterward, all samples were observed under a confocal microscope (LSM780, ZEISS, Germany). We then explored cell immunofluorescence by testing the vehicle and sh$Ca_v3.3$ in GelMA hydrogel via staining and observation using confocal microscopy.

Histological analyses

Next, we tested the developmental characteristics of GP, wild-type, and *Cacna1i*$^{-/-}$ mice by killing them and examining their knee joints. The joints were fixed with 4% paraformaldehyde at RT for 48 h before being decalcified with 10% ethylene diamine tetraacetic acid (EDTA) for 14–20 d prior to paraffin embedding. Continuous sections (thickness: 4 μm) were then acquired along the sagittal position, and we performed H&E and Safranin O-Fast Green staining.

To observe extracellular matrix (ECM) deposition in the GelMA hydrogel, we fixed samples cultured for 7, 14, and 21 d in 4% paraformaldehyde at RT for 15 min before embedding them in optimal cutting temperature compound (OCT) at 4 °C for 12 h. Then, the hydrogel was sliced into 15-μm sections using a cryomicrotome (Leica, CM1950, Germany) at −25 °C. These were then stained with Alcian Blue (Beyotime, China) and Alizarin Red S (Solarbio, China). Subsequently, ImageJ (NIH, USA) was used to quantify the relative intensity of Alcian Blue staining and the positive area of Alizarin Red S staining from images obtained under a microscope (ZEISS, AX10 Imager.A2, Germany). For Alcian Blue staining, the relative intensity was calculated by examining the ratio of the integrated density (IntDen) to the maximum integrated density (Max IntDen); here, all ratios were then normalized to a range between 0 and 1 using the maximum method. For Alizarin Red S staining, the ratio of the positive area was calculated by taking the unit field area that was occupied by an orange red complex.

Alkaline phosphatase (ALP) activity

Next, we assessed the mineralization process in the GelMA hydrogel. To do so, samples were cultured for 7, 14, and 21 d before being digested using 0.3 mg/mL GelMA hydrogel digesting solution (EFL Company, China). The resulting cell precipitate was obtained by centrifugation at 1000 r/min for 5 min and was used for subsequent ALP analyses. A cell lysis solution was prepared by incubating cells with 100-μL RIPA lysis buffer for 10 min. Subsequently, an ALP assay kit (Beyotime, China) was used to quantify ALP activity, with all procedures following the manufacturer's instructions. To obtain quantitative ALP measurements, the cell supernatant collected after a 20-fold dilution was transferred into a 96-well plate. After co-incubation of substrates and p-nitrophenol at 37 °C for 5 min, ALP activity was determined at a wavelength of 405 nm using a microplate reader (Multiskan SkyHigh, Thermo Scientific, USA). The total protein content of the cell lysate was determined in parallel using a bicinchoninic acid (BCA) assay kit (Beyotime, China). Here, ALP activity is expressed in diethanolamine (DEA) units, in which one DEA unit represents the amount of enzyme required to hydrolyze 1 μmol of p-nitrophenol in pH 9.8 DEA buffer at 37 °C. All data were presented in DEA units per mg total protein (μmol/(min·mg protein)) and were normalized against the minimum value.

Immunohistochemical staining

Next, to assess the expression of COL-II in two-layered hydrogels cultured for 21 d, samples were first sliced as described above. The slides were then treated with a solution containing 0.3% hydrogen peroxide in PBS to inhibit endogenous peroxidase activity. Subsequently, the slides were blocked using goat serum (1:100) before being incubated overnight at 4 °C with COL-II antibody (1:200; Affinity, China). After three washes with PBS, the slides were then exposed to a secondary antibody for 1 h at 37 °C. Following extensive rinsing in PBS, diaminobenzidine solution was used for slide development. Images were obtained from an AX10 IMAGER.A2 microscope (Zeiss, Germany). Here, all data were presented as integrated density and were normalized against the minimum value.

Statistical analyses

Quantitative results from scoring and image analyses were presented as mean ± standard deviation (SD). GraphPad Prism version 8.0 was used to perform *t*-tests or one-way analysis of variance (ANOVA) tests. Statistically significant differences are shown as follows: ns: $P > 0.05$, $^{*}P < 0.05$, $^{**}P < 0.01$, $^{***}P < 0.001$, and $^{****}P < 0.0001$.

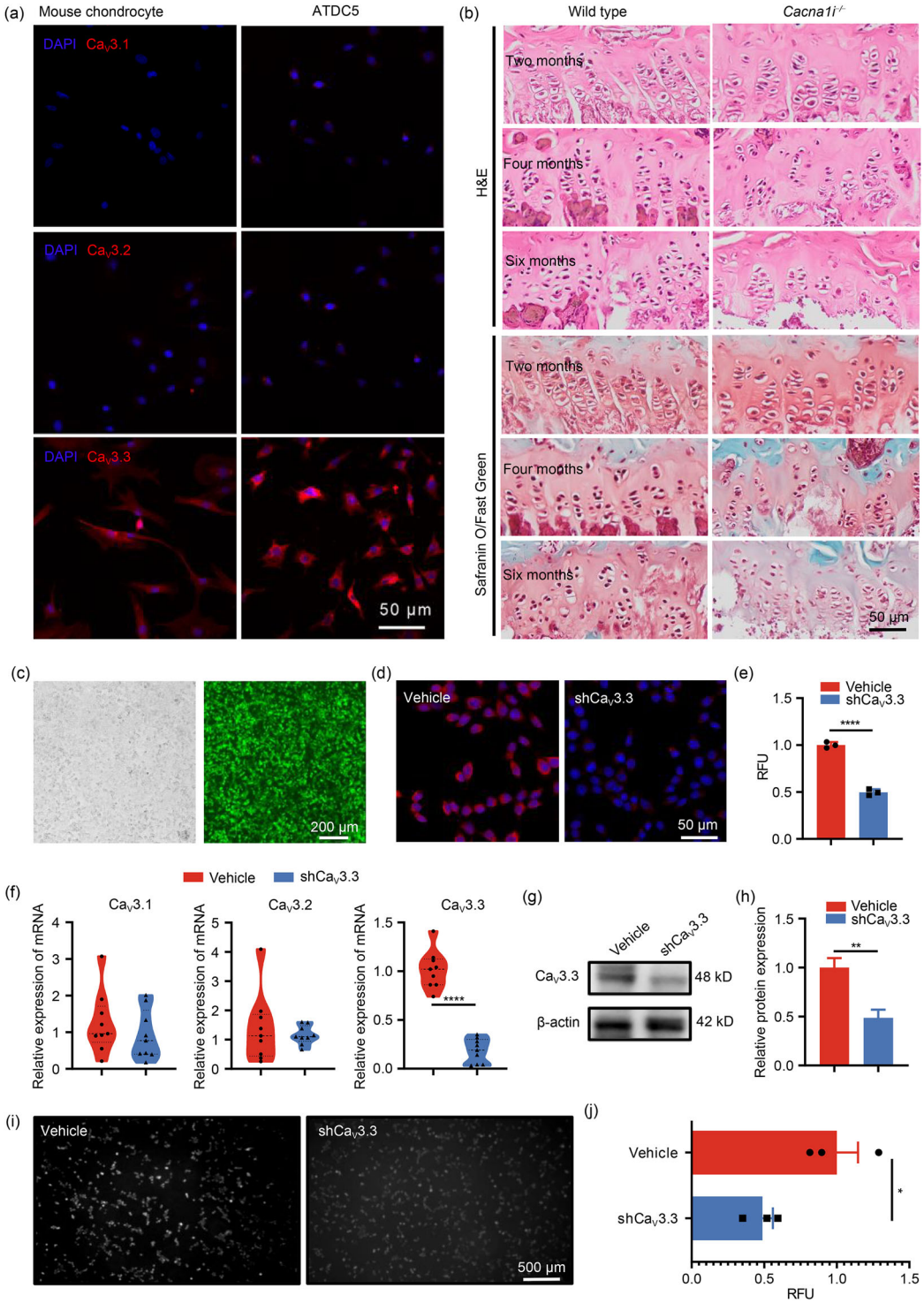

Fig. 1 $Ca_v3.3$ was negatively correlated with the hypertrophic differentiation of chondrocytes during EO. **a** Representative images of immunofluorescence staining against T-VDCC subtypes in mouse chondrocytes (n=3) and the ATDC5 cell line (n=3). **b** H&E and Safranin O/Fast Green staining in the GP of wild-type (n=3/time point) and *Col2*-CreERT *Cacna1i*$^{-/-}$ mice (n=3/time point). **c** Light and fluorescence microscope images of $Ca_v3.3$ interfered ATDC5 using HBLV-m-Cacna1i-shRNA-ZsGreen-PURO. **d** Representative immunofluorescence staining images against $Ca_v3.3$ in vehicle and sh$Ca_v3.3$, and **e** a corresponding semi-quantitative analysis. **f** Relative mRNA expression ratios of T-VDCC subtypes in vehicle and sh$Ca_v3.3$ groups. **g** Representative Western blotting results of $Ca_v3.3$ in vehicle and sh$Ca_v3.3$ groups, and **h** semi-quantitative analysis. **i** Calcium imaging and **j** quantitative analysis of vehicle and sh$Ca_v3.3$ groups. All data are presented as mean ± SD (n=3). $^{*}P < 0.05$, $^{**}P < 0.01$, and $^{****}P < 0.0001$. EO: endochondral ossification; T-VDCC: T-type voltage-dependent calcium channel; H&E: hematoxylin–eosin; GP: growth plate; SD: standard deviation; DAPI: 4',6-diamidino-2-phenylindole; RFU: relative fluorescent unit

Results

$Ca_v3.3$ was negatively correlated with hypertrophic differentiation of chondrocytes during EO

In primary mouse GP and ATDC5 chondrocytes, among the three subtypes of T-VDCCs, $Ca_v3.3$ showed the highest expression (Fig. 1a). Further H&E staining and Safranine O-Fast Green staining (Fig. 1b) were then performed on the distal tibial GP of wild-type and *Cacna1i*$^{-/-}$ mice aged 2, 4, and 6 months. These results showed that chondrocytes were arranged in an ordered manner in the GPs of the wild-type mice aged 2 and 4 months. In these mice, cellular morphology gradually transitioned from the round and dispersed chondrocytes present in the resting zone to columnar chondrocytes in the proliferation zone and eventually to terminal differentiation into a hypertrophic phenotype in the hypertrophic zone. However, wild-type GP chondrocytes in 6-month-old mice showed loss of order as well as GP maturation. This left few cells in the resting area and part of the proliferating zone. However, as shown in Fig. 1b, the arrangement of chondrocytes and the calcification process in 4-month *Cacna1i*$^{-/-}$ mice resembled those of 6-month-old wild-type mice. These data demonstrated that *Cacna1i* knockout can speed up the EO process in GP, which suggested that $Ca_v3.3$ was negatively correlated with the EO process and involved in the maturation of the mouse GP.

Next, we used sh$Ca_v3.3$ to explore the regulatory role of $Ca_v3.3$ in EO. As shown in Fig. 1c, ZsGreen fluorescence staining indicated that the interference sequence was successfully inserted into the DNA sequence of ATDC5 and was therefore stably expressed. Subsequently, immunofluorescence staining ($P < 0.0001$) (Figs. 1d and 1e), qRT-PCR ($P < 0.0001$) (Fig. 1f), and Western blotting ($P < 0.01$) (Figs. 1g and 1h) data verified that there was a significant decrease in $Ca_v3.3$ expression in stabilized sh$Ca_v3.3$. Furthermore, calcium imaging data showed a significant decrease in spontaneous calcium signaling in sh$Ca_v3.3$ ($P < 0.05$) (Figs. 1i and 1j).

The 5% GelMA hydrogel was printable at 15 °C and was suitable for sh$Ca_v3.3$ adhesion and proliferation

Next, we performed rheological tests at 15–27 °C to verify the suitability of a GelMA solution as a bioink for RT sh$Ca_v3.3$-loaded 3D bioprinting. The rapidly decreased storage modulus indicated that the 5% GelMA solution underwent the liquid–solid phase transition (Fig. 2a). We found that both the storage modulus and loss modulus decreased with increasing angular frequency, indicating that the material was plastic and processable within the linear viscoelastic range (Fig. 2b). Moreover, we selected a temperature of 15 °C, which was optimal for GelMA solution curability, for printing. Strain scanning of the material at this temperature showed that the storage modulus remained stable until 45% strain, indicating that a wide range of continuous extrusion speeds were applicable for printing (Fig. 2c). The diffusion diameter at 15 °C ($D_1 = (1.17 \pm 0.03)$ cm) was found to be significantly lower than that at 27 °C ($D_2 = (2 \pm 0.04)$ cm; $P < 0.0001$) (Figs. 2d and 2e), indicating that the hydrogel had significantly better bioprintability at 15 °C. Pipette tip squeezing and needle hanging tests indicated that the hydrogel possessed both good flowability and solidification at 15 °C (Fig. 2f). The swelling and degradation characteristics of the GelMA hydrogel (DAS = 60%, concentration = 5%) were then evaluated at 15 °C. The swelling ratio exhibited a rapid initial increase within the first 6 h, reaching equilibrium after 24 h at a significant weight gain of approximately 20% (Fig. 2g). In vitro degradation analysis using PBS containing collagenase type II revealed that the GelMA hydrogel underwent nearly complete degradation post-equilibrium swelling within 6 h (Fig. 2g).

Next, the sh$Ca_v3.3$-loaded 5% GelMA hydrogel scaffold was fabricated as a modeled cuboid scaffold measuring 5 mm × 5 mm × 1.5 mm at 15 °C, using an extruding pressure of 1 bar and an extruding speed of 7 mm/s. More than 90% of cells were still alive after the printing process, as was evident from the live and dead staining results (Fig. 2h). SEM examination of the hydrogel resulted in observation of a well-connected porous network with a uniform pore size, as observed along the *X*, *Y*, and *Z* axes. This structure provided a microenvironment amenable for cell adhesion and proliferation, as evidenced by further SEM images (indicated by white arrows) taken after 7 d of culturing (Fig. 2i and Fig. S1 in Supplementary Information).

The three-dimensional cultured 5% GelMA hydrogel was suitable for hypertrophy-related ECM deposition by sh$Ca_v3.3$

As shown in Fig. 3a, GO enrichment results showed that the DEGs identified following $Ca_v3.3$ knockdown (T_vs_C) were mainly concentrated in ECM-related pathways. Specifically, collagen containing ECM and endoplasmic reticulum-related genes were concentrated on the cellular component level, and ECM structural component and receptor activation-related genes were concentrated on the molecular function levels. Taken together, these results indicated that $Ca_v3.3$, a subtype of the T-VDCC membrane protein, affected the ECM secretion functions of chondrocytes. Interestingly, we detected DEGs in both plate cultures and GelMA hydrogels after $Ca_v3.3$ knockdown (Fig. 3b). Furthermore, a Sankey diagram revealed that more hypertrophy-related genes (i.e., *SHH* and *TGF-β*, among others) were enriched

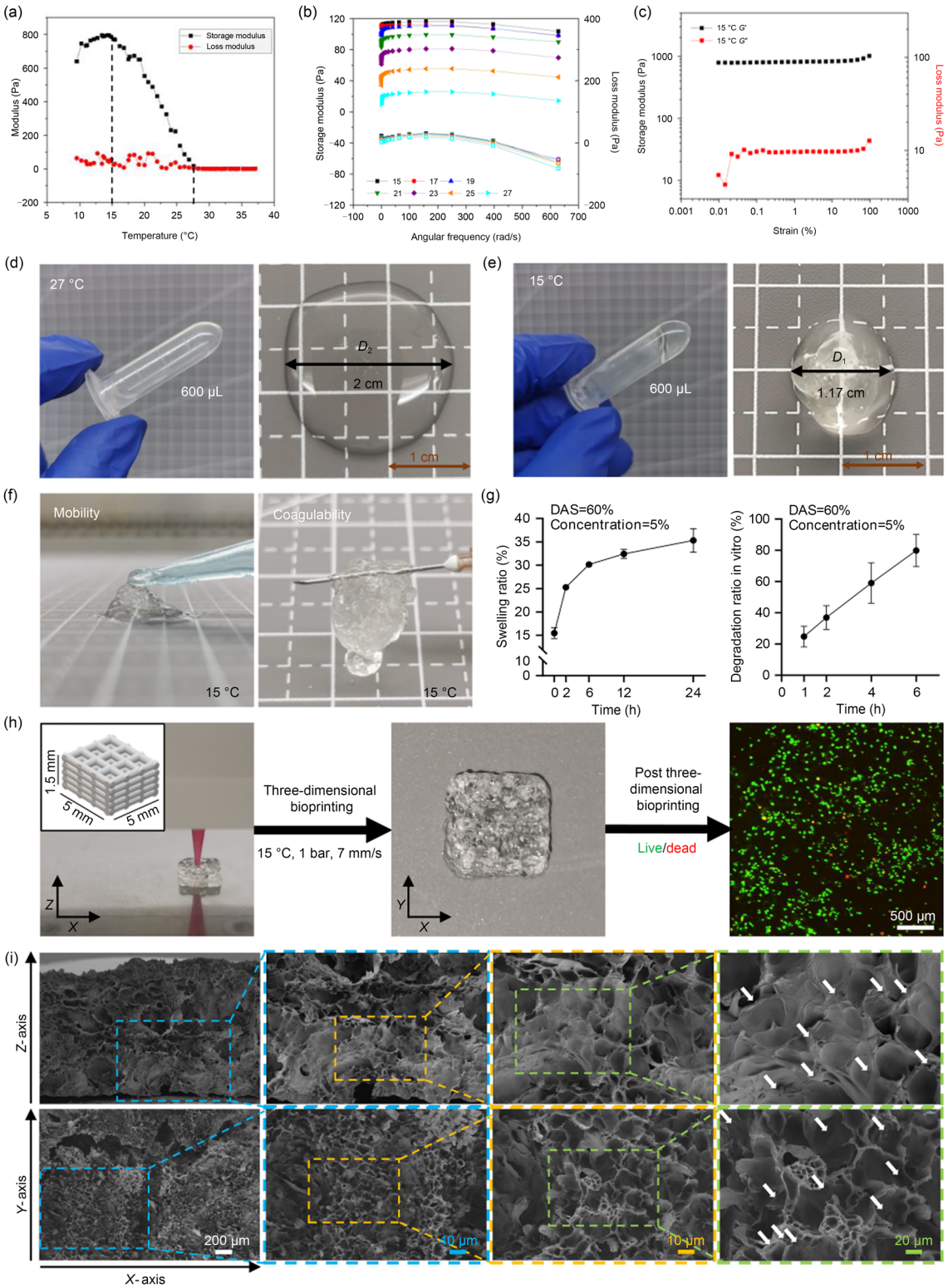

Fig. 2 Characterization of the physical parameters of the bioink. Shown are: **a** temperature, **b** frequency (storage modules: solid icon; loss modules: hollow icon), and **c** strain sweep of a 5% GelMA hydrogel. Diffusional appearance and diameter measurement of 600 μL GelMA at **d** 27 °C and **e** 15 °C. **f** Mobility and coagulability of the GelMA hydrogel at 15 °C. **g** Swelling ratio in PBS and the in vitro degradation ratio of collagenase type II of a GelMA hydrogel (data are presented as mean ± SD, $n = 3$). **h** A 3D bioprinting procedure using a model measuring 5 mm × 5 mm × 1.5 mm and subsequent live/dead staining of the $shCa_v3.3$ group in the bioink. **i** SEM images of cell attachment in a 3D printing GelMA hydrogel of the $shCa_v3.3$ group. 1 bar = 100 kPa. GelMA: gelatin methacryloyl; PBS: phosphate-buffered saline; SD: standard deviation; SEM: scanning electron microscopy; DAS: degree of amino substitution

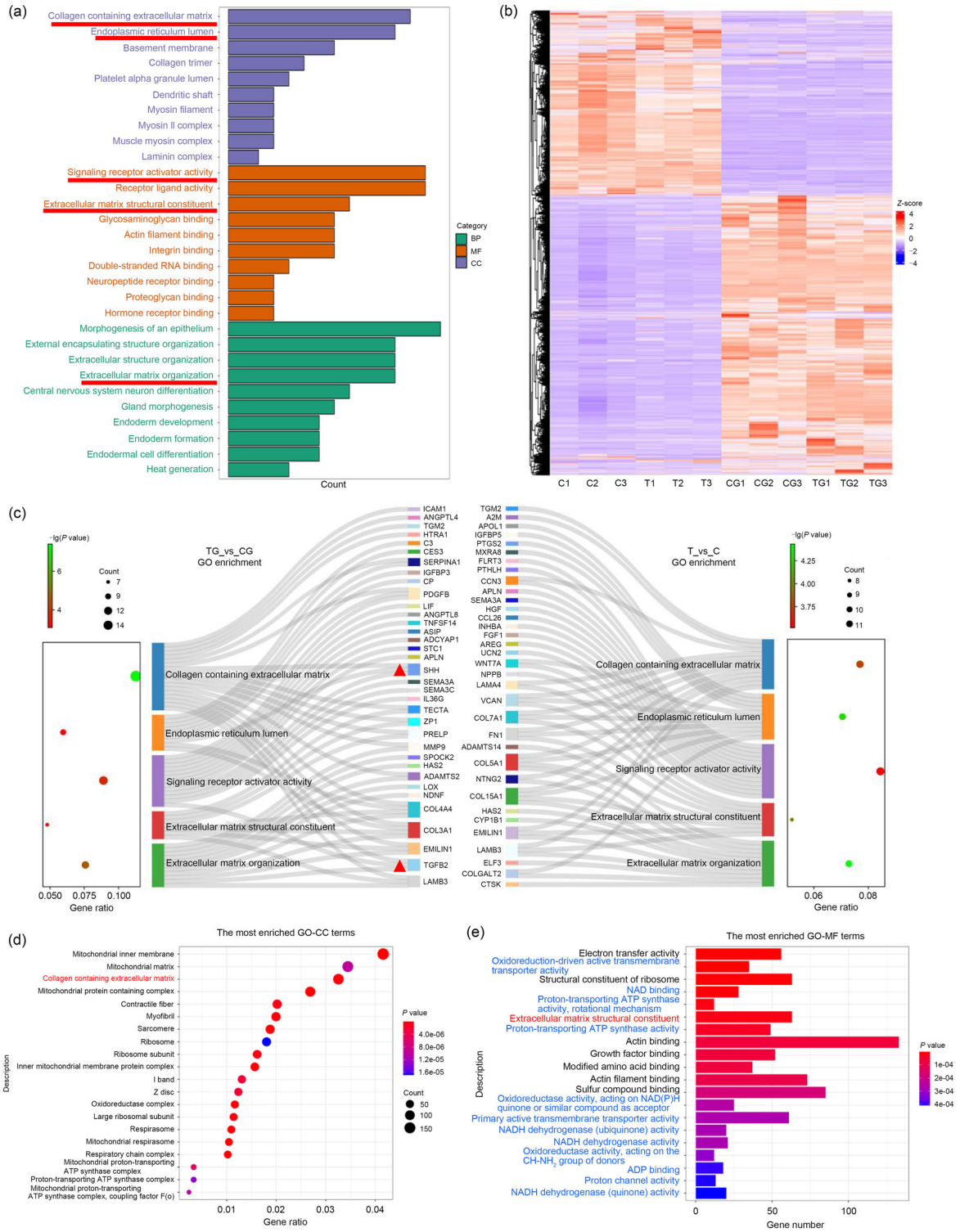

Fig. 3 The 3D culture environment was suitable for ATDC5 growth and hypertrophic differentiation-related ECM deposition. **a** GO enrichment analysis of DEGs post-$Ca_v3.3$ knockdown (T_vs_C). **b** Heat map of DEGs in 2D and 3D cell cultures. **c** Sankey diagram showing GO enrichment analysis results. This showed that the 3D culture promoted hypertrophic differentiation and associated gene expression in $Ca_v3.3$ knockdown ATDC5. **d** Bubble chart of cellular component terms, and **e** bar chart of molecular function terms identified by GO enrichment analysis as associated with DEGs. These results showed that the 3D culture promoted hypertrophic differentiation (TG_vs_T). DEGs were identified using the following diagnostic criteria: $P<0.05$ & $\log_2$ fold Change >1 or <−1. ECM: extracellular matrix; GO: gene ontology; DEGs: differentially expressed genes; BP: biological process; MF: molecular function; CC: cellular component

in the 3D culture (Fig. 3c). When compared to the TG and T groups (Figs. 3d and 3e), analysis of DEGs indicated that ECM-associated genes were enriched during 3D culturing. Meanwhile, as shown in Fig. 3e, energy metabolism pathways (shown in blue) were concentrated on the molecular function level. This finding indicated that the 3D culturing of the GelMA hydrogel showed superior energy metabolism, as evidenced by NAD/ATP binding, NADH dehydrogenase activity, and oxidoreductase activity, among other signs. In general, mRNA sequencing analyses revealed that the shCa$_v$3.3-loaded 5% GelMA hydrogel was highly suitable for simulating EO.

shCa$_v$3.3 in the GelMA hydrogel showed a hypertrophic phenotype and captured key characteristics of EO progress

As shown in Fig. 4a, both vehicle and shCa$_v$3.3 cells were in a normal proliferative state under long-term cultivation. After 1 d, about 76% of cells were in the proliferation state in both groups. Moreover, after 7 and 14 d, the positive cell rate of the vehicle group remained at about 60%, whereas that of the shCa$_v$3.3 group significantly decreased to about 43% ($P < 0.01$). Western blotting (Figs. 4b and 4c) showed significantly decreased expression of hyaline chondrocyte markers (i.e., COL-II, SOX-9, and ACAN) and significantly elevated expression of hypertrophic chondrocyte markers (i.e., COL-X, MMP-13, and RUNX-2) in shCa$_v$3.3. A similar observation was made using IF (Fig. 4d), confirming the phenotype transformation of ATDC5 from a hyaline chondrocyte to a hypertrophic chondrocyte.

In addition, proteoglycan intensity was detected by Alcian Blue (Fig. 5a) staining. Semi-quantitative analysis showed that the relative intensity of proteoglycan in shCa$_v$3.3 was weaker than that in the vehicle group at the 7-, 14-, and 21-d time points ($P < 0.0001$) (Fig. 5c). Moreover, Alizarin Red S staining indicated that calcium deposition increased with increasing culture period, whereas it was completely absent in the vehicle group (Fig. 5b). This was evident by the positive area of the shCa$_v$3.3 group significantly increasing over time to the point that it was larger than that of the vehicle group at 21 d of culturing ($P < 0.0001$) (Fig. 5d). Next, ALP quantitative analysis revealed a significant increase in ALP activity in shCa$_v$3.3 over time ($P < 0.001$), and this was significantly higher than that observed in the vehicle group by the 14- and 21-d time points ($P < 0.0001$). However, we also observed no significant difference between the shCa$_v$3.3 and vehicle groups by Day 7 (Fig. 5e). To simulate the transition from the proliferation area to the hypertrophy area of GP, we constructed a two-layered hydrogel. The surface layer comprised GelMA loaded with cells from the vehicle group to mimic the proliferation area, whereas the bottom layer comprised GelMA loaded with cells from the shCa$_v$3.3 group to represent the hypertrophy area. After 21 d of culturing, immunohistochemistry results showed increased deposition of COL-II in the surface layer (Fig. 5f). Semi-quantitative analysis revealed that the relative content of COL-II in the proliferative zone (surface) was more than three times greater than that in the hypertrophic zone (bottom) ($P < 0.0001$) (Fig. 5g).

Discussion

Improving our understanding of the molecular interactions that take place in the GP during EO may help us uncover the mechanisms responsible for long bone development and may provide a novel strategy for interventions in skeleton developmental diseases such as short stature and bone dysplasia [25–28]. However, in vivo research on EO has been restricted by multiple factors, such as unclosed GP, the necessity of extended experimental time periods, and indirect observation from discrete histological sections in an adult murine model [29]. To simulate EO in vitro, the present study verified the regulatory role of the T-VDCC subtype protein Ca$_v$3.3 in the hypertrophic differentiation of GP chondrocytes. Furthermore, we conducted a preliminary replication of the EO process in a 3D bioprinted GelMA hydrogel model.

Organoids are tissue engineered 3D cell culture systems that aim to emulate the multicellular relationships, spatial structures, and physiological functions of native organs, and hence provide an efficient platform for drug screening and basic research [6]. By using advanced biomaterials and 3D printing capabilities, advanced 3D bioprinting has successfully achieved the biomimetic construction of basic bone organotypic architecture. GelMA-based hydrogels are widely acknowledged to be an exceptional printable bioink material for bone organoids due to their remarkable biocompatibility, biodegradability, and flexible mechanical adjustability. The implementation of extruded 3D printing in our study not only facilitated enhanced printing accuracy via flow adjustment but also represents an important advance in the development of bionic construction technologies to be used to construct bone organoids [30–32]. Here, the osteochondral tissue that meets the native layered structure was printed using a microfluidic printing head, which enables the fabrication of scaffolds with very high shape fidelity and cell viability [33]. In addition, the differentiation of seed cells into osteoblasts can be accomplished through the use of drug-loaded hydrogel systems [34]. Nevertheless, precise imitation of the biological functioning of osteochondral units remains challenging. During GP development, hypertrophic differentiation of chondrocytes is induced by the TGF-β/BMP (bone morphogenetic protein), Wnt, and Hedgehog signaling pathways. Other signaling molecules are

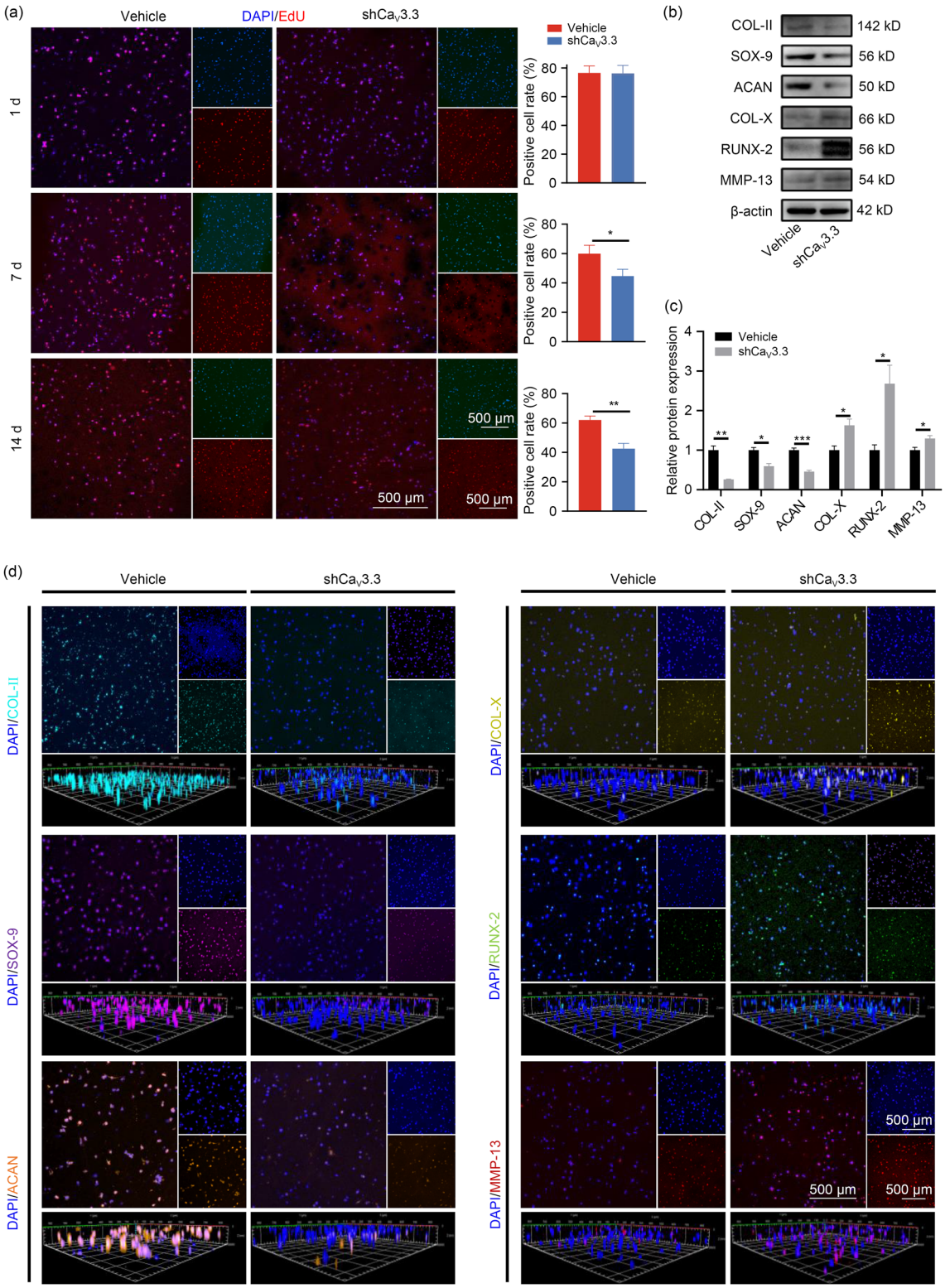

Fig. 4 $Ca_v3.3$ knockdown promoted hypertrophic differentiation of ATDC5 in a GelMA hydrogel. **a** In situ proliferation analysis by EdU staining on vehicle and $shCa_v3.3$ groups at the 1-, 7-, and 14-d time points. **b** Western blotting results and **c** semi-quantitative analyses of hypertrophic markers in vehicle and $shCa_v3.3$ groups. **d** Representative immunofluorescence staining images against hypertrophic markers in the vehicle and $shCa_v3.3$ groups. All data are presented as mean ± SD. $^{*}P < 0.05$, $^{**}P < 0.01$, and $^{***}P < 0.001$. GelMA: gelatin methacryloyl; EdU: 5-ethynyl-2-deoxyuridine; SD: standard deviation; DAPI: 4',6-diamidino-2-phenylindole

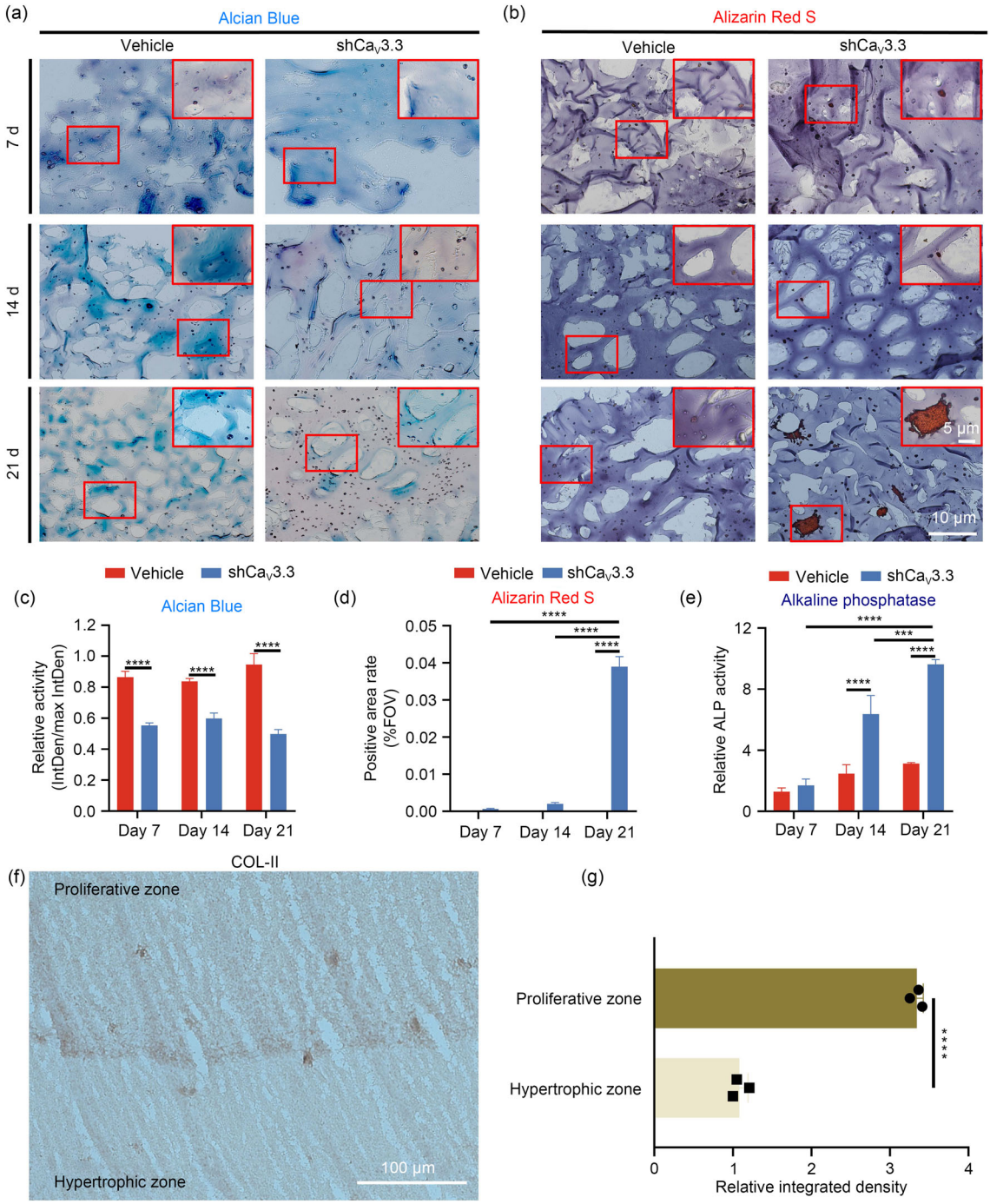

Fig. 5 $Ca_V3.3$ knockdown promoted EO-related ECM deposition in the GelMA hydrogel. **a** Alcian Blue staining of the vehicle and $shCa_V3.3$ groups at 7-, 14-, and 21-d time points. **b** Alizarin Red S staining of the vehicle and $shCa_V3.3$ groups at 7-, 14-, and 21-d time points. The quantitative analyses of **c** Alcian Blue, **d** Alizarin Red S, and **e** alkaline phosphatase of vehicle and $shCa_V3.3$ groups at 7-, 14-, 21-d time points after staining (n=3). **f** Immunohistochemical staining of COL-II was performed using a two-layered GelMA hydrogel that simulated the proliferation and hypertrophic zones. These were loaded with either vehicle or $shCa_V3.3$ cells. Finally, **g** shows semi-quantitative analysis (n=3). All data are presented as mean ± SD. $^{***}P < 0.001$ and $^{****}P < 0.0001$. EO: endochondral ossification; ECM: extracellular matrix; GelMA: gelatin methacryloyl; SD: standard deviation; FOV: field of view

also involved in osteogenic differentiation, including FGF, platelet-derived growth factor (PDGF), epidermal growth factor (EGF), insulin like growth factor (IGF) [35–39], transcription factors (e.g., RUNX-2, Osterix, and β-actin) [40], and various miRNAs (e.g., miR-335, miR-138 and miR-455-3p, among others) [41–44]. In addition, the in vitro simulation of these temporal and spatial regulatory circuits presents a key technical challenge.

Three-dimensional culturing is generally more suitable for in vitro model construction used to understand native cell physiological processes since it is better able to effectively mimic cell–cell and cell–ECM interactions that are found in vivo [45]. Moreover, the expression levels of key genes, including *COL-II* and *COL-X*, that are linked to cell differentiation can be significantly enhanced by a 3D system without any growth factors, and 3D systems have also been shown to have more active ECM remodeling than similar 2D culture systems [46]. Our mRNA sequencing analyses (Figs. 3d and 3e) also showed that the 3D culturing model reported here is highly suitable for obtaining differentiated phenotype cells and tracking ECM remodeling, and is also conducive for the exchange of nutrients and oxygen. The findings of previous studies align with this observation, since hydrogels have demonstrated the ability to establish a conducive microenvironment for cellular proliferation and differentiation within bone organoids. Furthermore, they facilitated tissue remodeling by promoting both intercellular and cell–ECM interactions [32]. Here, we investigated the developmental mechanisms of GP to identify potential regulatory targets, thereby providing an alternative perspective for the bone organoid development that differs from existing approaches in materials science and 3D printing engineering. However, the mechanisms responsible for electrophysiological microenvironment gradient transmission and precise regulation in the resting zone to the hypertrophy zone of GP were not clearly expounded in our model, which was not able to simulate the complete native development process from mesenchymal stromal cells to hypertrophic chondrocytes.

The regulation of skeleton maturation is usually triggered by specific physical and chemical cues and involves various regulators, including transcription factors, soluble mediators, extracellular matrices, and cell–cell and cell–matrix interactions [47–50]. In addition, voltage-gated ion channels such as the VDCCs located in hypertrophic zone chondrocytes play a key role in transmitting extracellular electrophysiological fluctuations into intracellular biological functions. A previous study indicated that VDCCs play an important role in GP maturation by regulating GP chondrocyte proliferation and differentiation [51]. However, the specific regulatory role of VDCC subtypes in EO has not yet been explored. Mutations in T-VDCCs might lead to a premature and/or shorter GP by shortening the height of the proliferative zone of the GP. This may occur by affecting the direction of mitosis, resulting in premature calcification. In the present study, the use of *Col2*-CreERT *Cacna1i*$^{-/-}$ mice permitted the advanced EO in GP to be observed at four months, as characterized by a disordered cell arrangement and the thinning of the GP. Taken together, these results indicated that $Ca_v3.3$ regulated the EO process during months 2–4 and implied that the electrophysiological microenvironment plays a role during GP maturation. During GP maturation, the phenotype of chondrocytes transformed from hyaline chondrocytes in the proliferation zone to hypertrophic chondrocytes in the hypertrophic zone [11, 12]. Chondrocytes are known to upregulate the expression of hypertrophic markers such as COL-X, MMP-13, and RUNX-2 [52, 53], induce angiogenesis via paracrine effects, and promote elongation and further calcification in vertebrate GP. Our histological section data revealed early hypertrophic differentiation of GP chondrocytes along with decreased cell density and proteoglycan intensity following tamoxifen injection. Furthermore, this phenomenon was verified in vitro by $Ca_v3.3$ knockdown in ATDC5 cell line using shRNA, thereby confirming that $Ca_v3.3$ may play a central role in the phenotypic transformation of GP chondrocytes.

Ca^{2+} is a key molecule that initializes many important cellular activities, including apoptosis, proliferation, and gene expression in many different cell types [54]. Large increases in the levels of free cytosolic Ca^{2+} concentration ($[Ca^{2+}]_i$) triggered by calcium channel-regulated extracellular Ca^{2+} influx and subsequent intracellular Ca^{2+} release from the intracellular store are messages interpreted by various downstream transcription factors (e.g., nuclear factor of activated T cells (Nfat), nuclear factor-κB (NF-κB), c-Jun N-terminal kinase 1 (JNK1), myocyte enhancer factor-2 (MEF2), and cAMP response element-binding protein (CREB)), whose activity can ultimately lead to a range of metabolic and signaling processes [55]. Our previous studies indicated that T-VDCCs may play an essential role in the initiation of extracellular Ca^{2+} influx and ECM deposition in chondrocytes [23] and that $Ca_v3.3$ may play a role in the hypertrophic differentiation of chondrocytes in early degenerated human articular cartilage [56]. In the present study, we further confirmed the expression of the $Ca_v3.3$ subtype in primary murine chondrocytes and the ATDC5 cell line and validated the role T-VDCCs played in the initiation of the extracellular Ca^{2+} influx, as evidenced by the significant decrease in free cytosolic Ca^{2+} concentration following $Ca_v3.3$ knockdown in ATDC5. In addition to the regulatory role $Ca_v3.3$ plays in the hypertrophic differentiation of GP chondrocytes, the disorganized cell arrangement of knockout mice may contribute to the accelerated ossification of GP. As shown in Fig. 1b, instead of a parallel aligned cell column, as can be observed in wild-type mice, an unparalleled or doubled cell

column was observed in *Cacna1i*$^{-/-}$ mice. This finding suggests that $Ca_v3.3$ may play an alternative role in the spatial polarity of the cartilaginous growth plate by mediating the mitotic direction of GP chondrocytes [57, 58].

Conclusions

In spite of its limitations, the present study preliminarily validated the strategy of simulating the EO process in bone organoids by regulating key molecules involved in hypertrophic differentiation of GP chondrocytes. Our data demonstrated that the $Ca_v3.3$ T-VDCC subtype is dominantly expressed in chondrocytes and is negatively correlated with the hypertrophic differentiation of chondrocytes during the EO process. In addition, a $Ca_v3.3$ knockdown chondrocyte-loaded GelMA hydrogel successfully captured the EO process and provides a functional bioink that may be capable of constructing layered and orderly mineralized GP organoids in the future. Our study therefore provides a potential target for regulating the EO process and a novel strategy for simulating EO in vitro.

Supplementary Information The online version contains supplementary material available at https://doi.org/10.1007/s42242-024-00287-1.

Acknowledgements This work was supported by the National Natural Science Foundation of China (No. 31800784), the Chongqing Key Laboratory of Precision Medicine in Joint Surgery (No. 425Z2138), the Chongqing Excellent Scientist Project (No. 425Z2W21), the Chongqing Natural Science Foundation General Project (No. cstc2021jcyj-msxmX0135), and the Chongqing Postdoctoral Research Project Special Fund (No. 2021XM3033). The authors thank the technical support in bioinformatics analysis offered by Knorigene Technologies.

Author contributions Conceptualization, ZW (Zhi Wang), XW, and YH; Methodology, ZW (Zhi Wang), XW, YH, and XYG; Investigation, ZW (Zhi Wang), XW, and YH; Formal analysis, ZW (Zhi Wang), JJY, and ZW (Zu Wan); Data processing, ZW (Zhi Wang) and ZLF; Writing—original draft, ZW (Zhi Wang); Writing—review & editing, all authors; Funding acquisition, XYG, GXC, and LY; Resources, XYG, GXC, and LY; Supervision, XYG, GXC, and LY.

Data availability The data generated in this study are available from the corresponding authors upon reasonable request.

Declarations

Conflict of interest All the authors declare that they have no conflict of interest.

Ethical approval The experiments were conducted in accordance with the National Institutes of Health Guide for the care and use of laboratory animals, and were approved by the animal ethics committee of the Third Military Medical University (Army Medical University), under approval number of AMUWEC20232652.

References

1. Hojo H, Ohba S (2019) Insights into gene regulatory networks in chondrocytes. Int J Mol Sci 20(24):6324. https://doi.org/10.3390/ijms20246324
2. Fernández-Iglesias Á, López JM, Santos F (2020) Growth plate alterations in chronic kidney disease. Pediatr Nephrol 35(3):367–374. https://doi.org/10.1007/s00467-018-4160-7
3. Haseeb A, Kc R, Angelozzi M et al (2021) SOX9 keeps growth plates and articular cartilage healthy by inhibiting chondrocyte dedifferentiation/osteoblastic redifferentiation. Proc Natl Acad Sci USA 118(8):e2019152118. https://doi.org/10.1073/pnas.2019152118
4. Buck DW, Dumanian GA (2012) Bone biology and physiology. Part II. Clinical correlates. Plast Reconstr Surg 129(6):950–956. https://doi.org/10.1097/PRS.0b013e31824ec354
5. Florencio-Silva R, da Silva Sasso GR, Sasso-Cerri E et al (2015) Biology of bone tissue: structure, function, and factors that influence bone cells. Biomed Res Int 2015:421746. https://doi.org/10.1155/2015/421746
6. Lancaster MA, Knoblich JA (2014) Organogenesis in a dish: modeling development and disease using organoid technologies. Science 345(6194):1247125. https://doi.org/10.1126/science.1247125
7. Chen SS, Chen X, Geng Z et al (2022) The horizon of bone organoid: a perspective on construction and application. Bioact Mater 18:15–25. https://doi.org/10.1016/j.bioactmat.2022.01.048
8. Rossi G, Manfrin A, Lutolf MP (2018) Progress and potential in organoid research. Nat Rev Genet 19(11):671–687. https://doi.org/10.1038/s41576-018-0051-9
9. Garreta E, Kamm RD, de Sousa C et al (2021) Rethinking organoid technology through bioengineering. Nat Mater 20(2):145–155. https://doi.org/10.1038/s41563-020-00804-4
10. Yun HH, Kim HJ, Jeong MS et al (2018) Changes of the growth plate in children: 3-dimensional magnetic resonance imaging analysis. Korean J Pediatr 61(7):226–230. https://doi.org/10.3345/kjp.2018.61.7.226
11. Oliveira Silva M, Gregory JL, Ansari N et al (2020) Molecular signaling interactions and transport at the osteochondral interface: a review. Front Cell Dev Biol 8:750. https://doi.org/10.3389/fcell.2020.00750
12. Lui JC (2020) Home for a rest: stem cell niche of the postnatal growth plate. J Endocrinol 246(1):R1–R11. https://doi.org/10.1530/JOE-20-0045
13. Lamandé SR, Ng ES, Cameron TL et al (2023) Modeling human skeletal development using human pluripotent stem cells. Proc Natl Acad Sci USA 120(19):e2211510120. https://doi.org/10.1073/pnas.2211510120
14. De Kinderen P, Meester J, Loeys B et al (2022) Differentiation of induced pluripotent stem cells into chondrocytes: methods and applications for disease modeling and drug discovery. J Bone Miner Res 37(3):397–410. https://doi.org/10.1002/jbmr.4524

15. Shao M, Teng XY, Guo X et al (2022) Inhibition of calcium signaling prevents exhaustion and enhances anti-leukemia efficacy of CAR-T cells via SOCE-calcineurin-NFAT and glycolysis pathways. Adv Sci 9(9):e2103508. https://doi.org/10.1002/advs.202103508
16. Kong F, You H, Zheng K et al (2021) The crosstalk between pattern-recognition receptor signaling and calcium signaling. Int J Biol Macromol 192:745–756. https://doi.org/10.1016/j.ijbiomac.2021.10.014
17. Fodor J, Matta C, Oláh T et al (2013) Store-operated calcium entry and calcium influx via voltage-operated calcium channels regulate intracellular calcium oscillations in chondrogenic cells. Cell Calcium 54(1):1–16. https://doi.org/10.1016/j.ceca.2013.03.003
18. Atsuta Y, Tomizawa RR, Levin M et al (2019) L-type voltage-gated Ca^{2+} channel $Ca_V1.2$ regulates chondrogenesis during limb development. Proc Natl Acad Sci USA 116(43):21592–21601. https://doi.org/10.1073/pnas.1908981116
19. Fan P, Pu D, Lv XH et al (2020) Cav 1.3 damages the osteogenic differentiation in osteoporotic rats by negatively regulating Spred 2-mediated autophagy-induced cell senescence. J Cell Mol Med 24(23):13863–13875. https://doi.org/10.1111/jcmm.15978
20. Ren RY, Guo JC, Chen YMF et al (2021) The role of Ca^{2+}/Calcineurin/NFAT signalling pathway in osteoblastogenesis. Cell Prolif 54(11):e13122. https://doi.org/10.1111/cpr.13122
21. Shao Y, Alicknavitch M, Farach-carson MC (2005) Expression of voltage sensitive calcium channel (VSCC) L-type $Ca_v1.2$ (α_{1C}) and T-type $Ca_v3.2$ (α_{1H}) subunits during mouse bone development. Dev Dyn 234(1):54–62. https://doi.org/10.1002/dvdy.20517
22. Lin SS, Tzeng BH, Lee KR et al (2014) $Ca_v3.2$ T-type calcium channel is required for the NFAT-dependent Sox9 expression in tracheal cartilage. Proc Natl Acad Sci USA 111(19):e1990–e1998. https://doi.org/10.1073/pnas.1323112111
23. Gong XY, Li GM, Huang Y et al (2019) Synergistically regulated spontaneous calcium signaling is attributed to cartilaginous extracellular matrix metabolism. J Cell Physiol 234(6):9711–9722. https://doi.org/10.1002/jcp.27657
24. Love MI, Huber W, Anders S (2014) Moderated estimation of fold change and dispersion for RNA-seq data with DESeq2. Genome Biol 15(12):550. https://doi.org/10.1186/s13059-014-0550-8
25. Rolian C (2020) Endochondral ossification and the evolution of limb proportions. WIREs Dev Biol 9(4):e373. https://doi.org/10.1002/wdev.373
26. Boudin E, Van Hul W (2018) Sclerosing bone dysplasias. Best Pract Res Clin Endocrinol Metab 32(5):707–723. https://doi.org/10.1016/j.beem.2018.06.003
27. Pauli RM (2019) Achondroplasia: a comprehensive clinical review. Orphanet J Rare Dis 14(1):1. https://doi.org/10.1186/s13023-018-0972-6
28. Linglart A, Merzoug V, Lambert AS et al (2017) Bone dysplasia. Ann Endocrinol 78(2):114–122. https://doi.org/10.1016/j.ando.2017.04.011
29. Corrò C, Novellasdemunt L, Li VSW (2020) A brief history of organoids. Am J Physiol Cell Physiol 319(1):C151–C165. https://doi.org/10.1152/ajpcell.00120.2020
30. Yang J, He H, Li D et al (2023) Advanced strategies in the application of gelatin-based bioink for extrusion bioprinting. Bio-Des Manuf 6(5):586–608. https://doi.org/10.1007/s42242-023-00236-4
31. Wu SL, Wu XM, Wang XH et al (2023) Hydrogels for bone organoid construction: from a materiobiological perspective. J Mater Sci Technol 136:21–31. https://doi.org/10.1016/j.jmst.2022.07.008
32. Zhang Y, Li GF, Wang J et al (2023) Small joint organoids 3D bioprinting: construction strategy and application. Small 20(8):e2302506. https://doi.org/10.1002/smll.202302506
33. Idaszek J, Costantini M, Karlsen TA et al (2019) 3D bioprinting of hydrogel constructs with cell and material gradients for the regeneration of full-thickness chondral defect using a microfluidic printing head. Biofabrication 11(4):044101. https://doi.org/10.1088/1758-5090/ab2622
34. Laomeephol C, Ferreira H, Kanokpanont S et al (2022) Osteogenic differentiation of encapsulated cells in dexamethasone-loaded phospholipid-induced silk fibroin hydrogels. Biomater Transl 3(3):213–220. https://doi.org/10.12336/biomatertransl.2022.03.005
35. Lowery JW, Rosen V (2018) The BMP pathway and its inhibitors in the skeleton. Physiol Rev 98(4):2431–2452. https://doi.org/10.1152/physrev.00028.2017
36. Chen GQ, Deng CX, Li YP (2012) TGF-β and BMP signaling in osteoblast differentiation and bone formation. Int J Biol Sci 8(2):272–288. https://doi.org/10.7150/ijbs.2929
37. Marcellini S, Henriquez JP, Bertin A (2012) Control of osteogenesis by the canonical Wnt and BMP pathways in vivo: cooperation and antagonism between the canonical Wnt and BMP pathways as cells differentiate from osteochondroprogenitors to osteoblasts and osteocytes. BioEssays 34(11):953–962. https://doi.org/10.1002/bies.201200061
38. Tsukasaki M, Komatsu N, Negishi-Koga T et al (2022) Periosteal stem cells control growth plate stem cells during postnatal skeletal growth. Nat Commun 13(1):4166. https://doi.org/10.1038/s41467-022-31592-x
39. Toosi S, Behravan J (2020) Osteogenesis and bone remodeling: a focus on growth factors and bioactive peptides. BioFactors 46(3):326–340. https://doi.org/10.1002/biof.1598
40. Augello A, De Bari C (2010) The regulation of differentiation in mesenchymal stem cells. Hum Gene Ther 21(10):1226–1238. https://doi.org/10.1089/hum.2010.173
41. Tomé M, López-Romero P, Albo C et al (2011) miR-335 orchestrates cell proliferation, migration and differentiation in human mesenchymal stem cells. Cell Death Differ 18(6):985–995. https://doi.org/10.1038/cdd.2010.167
42. Yang Z, Bian CJ, Zhou H et al (2011) MicroRNA hsa-miR-138 inhibits adipogenic differentiation of human adipose tissue-derived mesenchymal stem cells through adenovirus EID-1. Stem Cells Dev 20(2):259–267. https://doi.org/10.1089/scd.2010.0072
43. Eskildsen T, Taipaleenmäki H, Stenvang J et al (2011) MicroRNA-138 regulates osteogenic differentiation of human stromal (mesenchymal) stem cells in vivo. Proc Natl Acad Sci USA 108(15):6139–6144. https://doi.org/10.1073/pnas.1016758108
44. Zhang ZQ, Hou CH, Meng FG et al (2015) MiR-455-3p regulates early chondrogenic differentiation via inhibiting Runx2. FEBS Lett 589(23):3671–3678. https://doi.org/10.1016/j.febslet.2015.09.032
45. Skardal A, Shupe T, Atala A (2016) Organoid-on-a-chip and body-on-a-chip systems for drug screening and disease modeling. Drug Discov Today 21(9):1399–1411. https://doi.org/10.1016/j.drudis.2016.07.003
46. Ravi M, Paramesh V, Kaviya SR et al (2015) 3D cell culture systems: advantages and applications. J Cell Physiol 230(1):16–26. https://doi.org/10.1002/jcp.24683
47. Kolodkin-Gal I, Parsek MR, Patrauchan MA (2023) The roles of calcium signaling and calcium deposition in microbial multicellularity. Trends Microbiol 31(12):1225–1227. https://doi.org/10.1016/j.tim.2023.06.005
48. Qin L, Liu W, Cao HL et al (2020) Molecular mechanosensors in osteocytes. Bone Res 8(1):23. https://doi.org/10.1038/s41413-020-0099-y
49. Hasegawa K, Fujii S, Matsumoto S et al (2021) YAP signaling induces PIEZO1 to promote oral squamous cell carcinoma cell proliferation. J Pathol 253(1):80–93. https://doi.org/10.1002/path.5553

50. Umpierre AD, Wu LJ (2021) How microglia sense and regulate neuronal activity. Glia 69(7):1637–1653. https://doi.org/10.1002/glia.23961
51. Mancilla EE, Galindo M, Fertilio B et al (2007) L-type calcium channels in growth plate chondrocytes participate in endochondral ossification. J Cell Biochem 101(2):389–398. https://doi.org/10.1002/jcb.21183
52. Higashikawa A, Saito T, Ikeda T et al (2009) Identification of the core element responsive to runt-related transcription factor 2 in the promoter of human type X collagen gene. Arthritis Rheum 60(1):166–178. https://doi.org/10.1002/art.24243
53. Li YW, Trivedi V, Truong TV et al (2015) Dynamic imaging of the growth plate cartilage reveals multiple contributors to skeletal morphogenesis. Nat Commun 6(1):6798. https://doi.org/10.1038/ncomms7798
54. Missiaen L, Robberecht W, van den Bosch L et al (2000) Abnormal intracellular Ca^{2+} homeostasis and disease. Cell Calcium 28(1):1–21. https://doi.org/10.1054/ceca.2000.0131
55. Smedler E, Malmersjö S, Uhlén P (2014) Network analysis of time-lapse microscopy recordings. Front Neural Circ 8:111. https://doi.org/10.3389/fncir.2014.00111
56. Gong XY, Xie WB, Wang B et al (2017) Altered spontaneous calcium signaling of in situ chondrocytes in human osteoarthritic cartilage. Sci Rep 7(1):17093. https://doi.org/10.1038/s41598-017-17172-w
57. Abad V, Uyeda JA, Temple HT et al (1999) Determinants of spatial polarity in the growth plate. Endocrinology 140(2):958–962. https://doi.org/10.1210/endo.140.2.6513
58. Li YW, Dudley AT (2009) Noncanonical frizzled signaling regulates cell polarity of growth plate chondrocytes. Development 136(7):1083–1092. https://doi.org/10.1242/dev.023820